Long range path planning using an aircraft performance model for battery powered sUAS equipped with icing protection system

Anthony Reinier Hovenburg, *Student Member, IEEE,* Fabio Augusto de Alcantara Andrade, *Member, IEEE,* Richard Hann, Christopher Dahlin Rodin, *Student Member, IEEE,* Tor Arne Johansen, *Senior Member, IEEE,* and Rune Storvold, *Member, IEEE*

***Abstract*—Earlier studies demonstrate that en-route atmospheric parameters, such as winds and icing conditions, significantly affect the safety and in-flight performance of unmanned aerial systems. Nowadays, the inclusion of meteorological factors is not a common practice in determining the optimal flight path. This study aims to contribute with a practical method that includes meteorological forecast information in order to obtain the most energy efficient path of a fixed-wing aircraft. The Particle Swarm Optimization based algorithm takes into consideration the aircraft performance, including the effects of en-route winds and the power required for active electro-thermal icing protection systems to mitigate the effects of icing. As a result, the algorithm selects a path that will use the least energy to complete the given mission. In the scenario evaluated with real meteorological data and real aerodynamic parameters, the battery consumption of the optimized path was 52% lower than the standard straight path.**

***Keywords*—Path-planning, icing protection systems, unmanned aerial systems, particle swarm optimization.**

I. Introduction

SMALL Unmanned Aerial Systems (sUAS) have become versatile tools that can be used in a broad spectrum of missions. The rapid growth of the use of sUAS is justified by their endurance, reduced cost, rapid deployment and flexibility. This flexibility is mainly due to the many types of sensors that can be mounted on sUAS, enabling them to be used in many different applications, such as surveillance, reconnaissance, search and rescue, delivery, photogrammetry, inspection, among others. In addition, they offer reduced risk for humans and impact on the environment, when compared to manned aircraft.

A next and necessary step for the continuous evolution of sUAS technology is to enable safe autonomous missions also in adverse weather conditions. For this to be possible, effects of wind and icing on the aircraft performance must be addressed, controlled and taken into consideration by the path planning algorithm to decide if it is worth it to face the adverse weather conditions or to take a detour in order to avoid exposing the sUAS to this.

Scientific literature on path planning of sUAS is abundant. In [1] a comparative analysis of four three dimensional path planning algorithms based on geometry search was done. The algorithms compared were Dijkstra, Floyd, A* and Ant Colony. Run time and path length were the two analyzed aspects. In [2], the author used the Voronoi diagram to produce routes minimizing their detection by radar, while in [3] the Rapidly Exploring Trees (RTTs) were used with a smoothing algorithm based on cubic spiral curves for collision-free path planning. Optimization techniques are also adopted, as Genetic Algorithms [4], MILP [5] and Particle Swarm Optimization [6], where the author used the method to minimize the UAS path's length and danger based on the proximity of threats.

Atmospheric wind usually constitute 20-50% of the airspeed of sUAS [7]. Therefore, it affects the aircraft's in-flight performance significantly. In [8], a sophisticated method was described where Model Predictive Control (MPC) was employed for path planning optimization including the effects of uniform wind. In [9], the author used Markov Decision Process to optimize the unmanned aerial vehicle's path, integrating the uncertainty of the wind field into the wind model. The goal of the algorithm was to minimize the energy consumption and time-to-goal. A similar approach was chosen in [10], where the Ant Colony Optimization (ACO) technique was used to optimize the path by minimizing the travel time considering the effects of an uniform wind.

Most of the works about path planning of sUAS that takes the wind into consideration use an uniform wind distribution. This information is often used in a simplified model when calculating the effects of the wind on the energy consumption. However, in [11], aircraft performance was successfully included, with the assumption of a constant wind field. In recent literature a nonuniform wind distribution in addition to an aircraft performance model was used. That is the case in [12], where the flight path was optimized so that sUAS was guaranteed to be able to reach a pre-designated safe landing stop. This was done by continuously calculating the remaining range considering the remaining battery capacity in case of an engine failure. In that study a wind map with nonuniform wind distribution was used in the calculations of the maximum range of the sUAS. Also using a nonuniform wind distribution, [13] proposed a two-dimensional optimization algorithm to

A. R. Hovenburg, F. A. A. Andrade, R. Hann, C. D. Rodin, T. A. Johansen and R. Storvold are with the Department of Engineering Cybernetics, Norwegian University of Science and Technology, Trondheim, Norway (e-mail: hovenburg@ieee.org; fabio@ieee.org; richard.hann@ntnu.no; cdahlin@ieee.org; tor.arne.johansen@ntnu.no; rust@norceresearch.no).

F. A. A. Andrade and R. Storvold are with the Drones and Autonomous Systems, NORCE Norwegian Research Centre, Tromso, Norway.

F. A. A. Andrade is with the Graduate Program in Electrical Engineering, Federal Center of Technological Education of Rio de Janeiro, Rio de Janeiro, Brazil.

find the path between two points with the minimum energy consumption. By being aware of the wind map valid for a given altitude, it was possible to choose a path where the wind was used favorably for energy savings for that flight level.

One of the most important meteorological constraints for sUAS mission planning is atmospheric icing. This hazard is also called in-cloud icing and occurs when an airframe travels through a cloud containing supercooled liquid droplets. When these droplets collide with the airframe they freeze and result in surface icing that grow over time into ice horns that can significantly alter the wing shape. Even small ice accretions have been shown to be able to decrease the aerodynamic performance of a wing dramatically [14] [15].

The icing hazard is a well-researched topic for general aviation, but little attention has been given to this topic until the recent years for sUAS – although the issue has already been identified during the 1990s [16]. UAS icing is in many ways similar to icing on large aircrafts, but also exhibits significant differences when it comes to flight velocities, airframe size, mission profiles, and weight restrictions. In particular, sUAS typically operate at Reynolds numbers an order of magnitude lower compared to general aviation which causes differences in the flow regime [17].

Modeling of icing effects on sUAS have shown that icing results in a degradation of aerodynamic performance. Ice accretions on the leading edge of the lifting surfaces can decrease lift, increase drag, and initiate earlier stall [18]. The degree of the degradation seems strongly linked to the prevailing meteorological conditions. In addition, icing has also shown to have detrimental effects on static and dynamic stability. In summary, icing is a severe hazard, especially for sUAS, and it is common practice to avoid flying in icing at all costs.

An icing protection system (IPS) can be used to mitigate this restriction of the flight envelope. In the scope of this work, an electro-thermal system will be investigated [19] [20]. This system consists of heating zones on the leading edge of the lifting surfaces that are activated when the aircraft enters an icing cloud. The IPS can run in two different modes. In anti-icing mode, the system will continuously heat the leading edge to inhibit the build-up of any ice. In de-icing mode, the systems operates in a cyclic way, allowing for the accumulation of a small amount of ice over a time of 90 s, followed by the removal of the ice by activating the heating zones for 30 s. Typically, the de-icing mode will require lower power requirements compared to anti-icing, but will also results in performance degradation during the ice accumulation cycles [21].

As weather conditions often varies for geographic location and altitude, it is important that the path planning algorithm is able to allow altitude changes during the flight. Consequently, the terrain profile must be taken into consideration and treated as an obstacle by the algorithm. This was previously implemented by [22], where the PSO and Parallel GA optimization techniques were compared when used to find the best trajectory by minimizing a cost function based on the path length and average altitude, including a penalization in the cases when the path has parts under the terrain.

In this study, a path planning algorithm is proposed to find an optimal path between a chosen origin and destination allowing both changes in course and altitude. It is important to stress to the reader that this work does not present innovation on the path planning method itself neither on the optimization technique, but rather contributes by integrating several elements in the cost function, some of which are novel and others that are normally studied individually in the literature. These factors include: the icing protection system usage, which is a very novel solution that enables sUAS to fly under icing conditions; nonuniform horizontal wind, that is a major issue on sUAS operations and has only recently been studied; terrain elevation profile, that is a fundamental factor that has already been included in many studies; the aircraft performance model, which brings more realistic and accurate calculations of the propulsion required power according to the aircraft platform and environmental parameters; and battery discharge properties, which is a relevant factor as sUAS are typically powered by electric batteries and the discharge rates vary according to the remaining capacity.

Therefore, this work contributes to the field by proposing a tool that can be used to plan the sUAS mission and to evaluate different possible scenarios, in order to assist the decision making. The highlights of the contributions are summarized as the following:

- Integration of different models such as aircraft performance, terrain elevation, nonuniform wind and battery potential in the cost function;
- Inclusion of the effects of performance degradation during the ice accumulation cycles on the aircraft performance;
- Inclusion of the icing protection system model and its effects on the energy consumption in the cost function; and
- Simulations for a scenario with real weather and elevation data, as well as real aircraft, battery and icing protection system parameters.

The work is organized as follows: after the introduction, Section II contains the aircraft performance model and the battery performance model is described in Section III. The meteorological and elevation data are described in Section IV. The path planning algorithm and its cost function are described in Section V. The case study, including the aircraft and icing protection system parameters are presented in Section VI. The results are discussed in Section VII and conclusions are given in Section VIII.

II. Aircraft performance model

In this chapter the aircraft performance model is presented with all the equations that are needed for the calculation of the required power to propel the aircraft in given atmospheric conditions and for a desired maneuver.

A. Pressure

The pressure (p in [Pa]) is calculated from the aircraft altitude by using the barometric formula with subscript 0, that

is valid from sea level up to 11000 m of altitude:

$$p(h) = p_0 \left[\frac{T_0}{T_0 + L_0(h - h_0)} \right]^{\frac{g_0 M}{R L_0}} \quad (1)$$

where h is the altitude in [m], p_0 is the standard pressure at sea level of 101325 Pa, T_0 is the standard temperature at sea level of 288.15 K, L_0 is the standard temperature lapse rate for subscript 0 of -0.0065 K/m, h_0 is the altitude at sea level of 0 m, R is the molar gas constant of 8.314472 Jmol^{-1}K^{-1}, M is the molar mass of Earth's air of 0.0289644 kg/mol and g_0 is the gravitational acceleration at sea level of 9.80665 m/s^2.

The values of the constants are taken from the International Standard Atmosphere (ISA) mean sea level conditions [23].

B. Air Density

The density of air (ρ in [kgm^{-3}]) is an atmospheric property which significantly affects the aerodynamic forces.

To calculate the air density, the ideal gas law is used:

$$\rho(p, T) = \frac{p}{R_d T}, \quad (2)$$

where p is the pressure in [Pa] given by Eq. 1, T is the air temperature in [K] and R_d is the specific gas constant for dry air of 287.058 Jkg^{-1}K^{-1}.

C. Power Required

Assuming that the lift (Fig. 1) is high enough to compensate its opposite weight component to keep the aircraft in the air, it is necessary to provide a power high enough to: provide a thrust to overcome the drag force and the weight's component tangent to the aircraft's trajectory; and to move the aircraft forward in its trajectory with an excess thrust. Therefore, the required propulsive power is given by multiplying the required thrust by the desired airspeed:

$$P_{req}(T_{req}, v_a) = T_{req} v_a \quad (3)$$

where P_{req} is the required propulsive power in [W] given by Eq. 3, v_a is the airspeed in [m/s] and T_{req} is the required thrust in [N], which is given by:

$$T_{req}(D, \theta) = D + W sin(\theta) \quad (4)$$

where D is the drag force in [N] given by Eq. 5, W is the aircraft weight in [N] and θ is the climb angle in [rad].

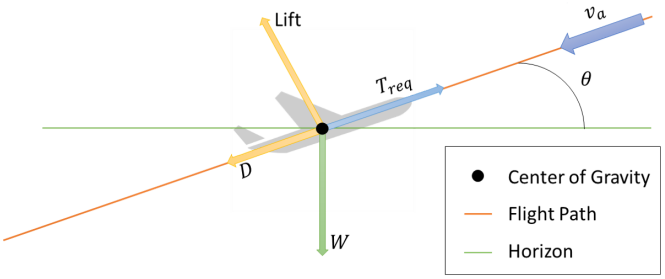

Fig. 1. 2-D representation of an aircraft in a straight flight.

Hence, when the aircraft is cruising (θ is equal to zero), this results in $sin(\theta)$ being equal to zero. In this case, the weight is normal to the drag force and tangent to the lift.

As the drag force is dependent on the body's size (e.g. the wing surface), the air density and the airspeed, the equation for drag force D is derived by dimensional analysis following the Buckingham's π-Theorem:

$$D(\rho, v_a, C_D) = 0.5 \rho v_a^2 S C_D \quad (5)$$

where ρ is the air density in [kgm^{-3}] given by Eq. 2, v_a is the airspeed in [m/s], S is the wing surface area in [m^2] and C_D is the drag coefficient, given by Eq. 8.

For an aircraft equipped with propellers, the engine's required power (P_{shaft}) is obtained dividing the propulsive required power (P_{req} in W, given by Eq. 3) by the propeller efficiency (η_p):

$$P_{shaft}(P_{req}) = \frac{P_{req}}{\eta_p}. \quad (6)$$

From the descent slope which no propulsion power is required, the aircraft's motor is assumed to be completely shut off and the on-board systems, except for the icing protection systems, are assumed to use insignificant amounts of energy. Therefore, the energy consumption in this case is assumed to be equal to the energy consumption of the icing protection requirements. This is possible for an electric powered aircraft that does not need to keep an engine running during the entire mission. However, the maximum descent angle needs to be chosen so that sufficient lift is provided for airspeed values that are in the range of predefined accepted values of the desired airspeed.

1) Aerodynamic Coefficients: To be able to calculate the drag force, which characterizes the power required to propel the sUAS, it is necessary to first calculate the drag and lift coefficients (C_D and C_L respectively).

In common A-to-B missions the aircraft is expected to primarily be flying in a horizontal straight flight, and performs a limited amount of turns. These turns depend on the path optimization, however the turns denote on a relatively small part of the entire path. Therefore, the effects of turns (circling flights) are not considered in the following calculations. This holds valid for "A-to-B" missions, and not for other mission types, such as loitering.

In addition, and with respect to the mission profile, the aircraft is assumed to follow a steady motion flight path, trust angle is zero, and the angle of attack is small, typically ranging between -4 and 10 deg.

The lift coefficient for straight flight is given by [24] as:

$$C_L(\theta, \rho, v_a) = \frac{2W \cos(\theta)}{\rho S v_a^2}, \quad (7)$$

where v_a is the airspeed in [m/s], W is the aircraft weight in [N], θ is the climb angle in [rad], ρ is the air density in [kgm^{-3}] given by Eq. 2 and S is the wing surface area in [m^2].

In this study, the drag coefficient (C_D) as a function the lift coefficient (C_L) was derived by a curve fitting process that aims to find a polynomial equation that represents the true drag polar, typically acquired from wind tunnel experiments or

Computational Fluid Dynamics (CFD) simulations. AOA data ranging from -4 to 8 deg was used in the curve fitting process. To derive a valid polynomial equation, it is necessary to first define the range of the lift coefficient where the equation will be valid. This domain can be calculated by finding the lowest and highest lift coefficient ($C_{L_{min}}$ and $C_{L_{max}}$), respectively, for the mission and aircraft constraints, such as minimum and maximum accepted airspeed (v_a), minimum and maximum accepted climb angle (θ) and minimum and maximum air density (ρ). C_D is therefore a function of C_L:

$$C_D(C_L) = f(C_L), \tag{8}$$

where f is the fitted function.

D. Ground speed

The airspeed is the speed of the aircraft with relation to the mass of air in which it is flying. Therefore, when the aircraft climbs or descends, it is possible to calculate the projection of the airspeed on the horizontal axis (Fig. 2), with the assumption of the absence of vertical wind, by:

$$v_h(v_{h_x}, v_{h_y}) = \sqrt{v_{h_x}^2 + v_{h_y}^2}, \tag{9}$$

with x and y components of the horizontal airspeed (v_h) given by:

$$\begin{aligned} v_{h_x}(v_a, \psi, \theta) &= v_a \sin(\psi)\cos(\theta), \\ v_{h_y}(v_a, \psi, \theta) &= v_a \cos(\psi)\cos(\theta) \end{aligned} \tag{10}$$

where v_a is the airspeed in [m/s], ψ is the heading in [rad] (Eq. 12) and θ is the climb angle in [rad].

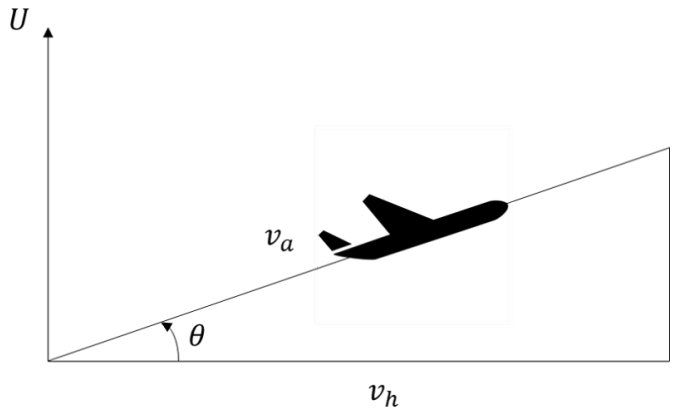

Fig. 2. Representation of side view of the aircraft.

The presence of wind affects the aircraft's travelled trajectory (Fig. 3). The travelled trajectory is subject to the aircraft's ground speed (v_{gs} in [m/s]), which is the aircraft's speed relative to the ground and calculated by:

$$\begin{aligned} &v_{gs}(v_{h_x}, v_{h_y}, v_{wind_x}, v_{wind_y}) = \\ &\sqrt{(v_{h_x} + v_{wind_x})^2 + (v_{h_y} + v_{wind_y})^2}, \end{aligned} \tag{11}$$

where v_h is the horizontal airspeed in [m/s] and v_{wind} the wind speed in [m/s].

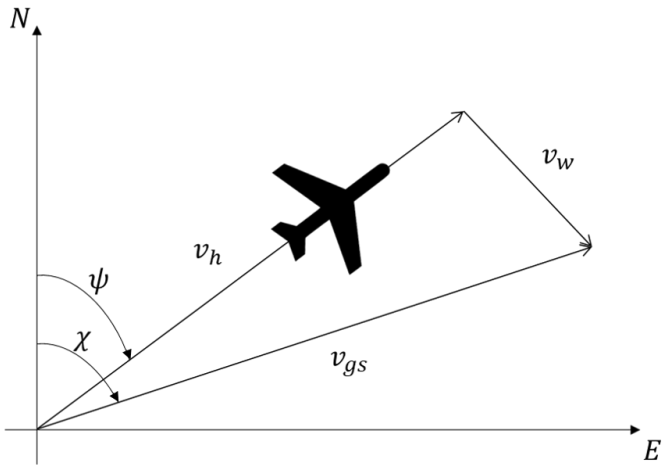

Fig. 3. Wind triangle.

The heading angle (ψ) is the direction where the aircraft is pointing to. Its angle starts at the North direction ($\psi = 0$) and increases towards East. It is, therefore, given by:

$$\psi(\chi, v_{wind}, v_a, \psi_{wind}) = \chi - \arcsin\left(\frac{v_{wind}}{v_a \sin(\psi_{wind} - \chi)}\right), \tag{12}$$

where the course angle (χ in [rad]) is the travel direction relative to the ground, with the wind speed (v_{wind} in [m/s]) given by:

$$v_{wind}(v_{wind_x}, v_{wind_y}) = \sqrt{v_{wind_x}^2 + v_{wind_y}^2}, \tag{13}$$

and with the wind heading angle (ψ_{wind} in [rad]) given by:

$$\psi_{wind}(v_{wind_x}, v_{wind_y}) = \arctan2(v_{wind_x}, v_{wind_y}). \tag{14}$$

III. Battery performance model

Modern electric batteries have become dominant power sources within sUAS, mainly because of their simplicity, and relatively high peak power output. Common battery types, such as lithium-based cells, are rechargeable and durable, which makes them suitable for sUAS operations.

Electric batteries have variable potential according to the remaining capacity. [25] presented a simple model for open-circuit potential determination. With this model, it is possible to calculate the battery potential with respect to the current being drawn. Lately, [26] derived the model equations to calculate the rate of discharge for a constant-power. [24] modelled the battery potential (V_{oc} in [V]) based on [25] as (Fig. 4):

$$V_{oc}(C, V_o) = V_o - \left(\frac{\kappa C_{cut}}{C_{cut} - C}\right) + Ae^{-BC}, \tag{15}$$

where C_{cut} is the capacity discharged at cut-off in [Ah], C is the capacity discharged in [Ah], $A = V_{full} - V_{exp}$ and $B = 3/C_{exp}$ where V_{full} is the fully charged potential in [V]. Additionally, V_{exp} is the potential at the end of the exponential range in [V], and C_{exp} is the capacity discharged at the end

of the exponential range in [Ah], with the Polarization Voltage (κ in [V]):

$$\kappa = \frac{(V_{full} - V_{nom} + A(e^{-BC_{nom}} - 1))(C_{cut} - C_{nom})}{C_{nom}}, \tag{16}$$

where V_{nom} is the potential at the end of the nominal range in [V], C_{nom} is the capacity discharged at the end of the nominal range in [Ah], and with battery constant potential (V_o in [V]):

$$V_o(I_{eff}, V_{oc}) = V_{full} + \kappa + (R_C I_{eff}) - A, \tag{17}$$

where R_C is the internal resistance in [Ohms] and I_{eff} is the effective discharge current in [A].

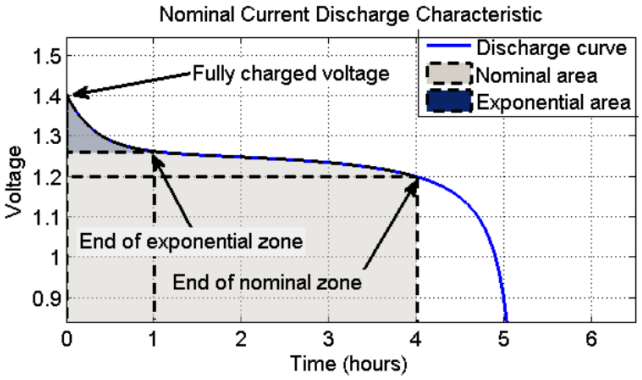

Fig. 4. Battery discharge curve. (From [25])

In this study, the power is considered constant during the discretization step, and, therefore, the effective discharge current is the variable to be calculated. As a result, the Trembley's equations were manipulated to accommodate obtaining the effective discharge current for a given power. From Ohm's law, the effective current (I_{eff} in [A]) is given by:

$$I_{eff}(V_{oc}) = \frac{P_{eff}}{V_{oc}}, \tag{18}$$

with the potential (V_{oc} in [V]) being obtained by solving the nonlinear equation:

$$V_{oc}^{n+1} - \left(V_{full} + \kappa - A - \frac{\kappa C_{cut}}{C_{cut} - C} + Ae^{-BC}\right)V_{oc}^{n} - R_C I_{rated}^{1-n} P_{eff}^{n} = 0, \tag{19}$$

where n is the battery-specific Peukert's constant and I_{rated} is the maximum battery rated current in A.

Note that to obtain the potential (V_{oc}), it is necessary to solve the nonlinear Eq. 19. The valid solution will be in the range from the cut-off potential (V_{cut}) to the fully charged potential (V_{full}).

IV. Meteorological and Elevation Data

This work aims to allow sUAS operations in adverse weather conditions. Therefore, meteorological forecast data needs to be considered. This data is used in the calculation of the total aircraft energy consumption, as it affects the aircraft's in-flight performance. Additionally, the meteorological conditions define when the icing protection systems are to be used, and how much power is required to mitigate the adverse effects of aircraft icing. Finally, the elevation data is of importance as the path planning algorithm optimizes the sUAS' altitude, and therefore it is vital to ensure a minimum terrain clearance in the aircraft's planned path.

A. Meteorological parameters

In Table I the downloaded parameters are shown. The wind and air temperature parameters are implemented directly in the form that they were supplied in. Other parameters were modified due to unit compatibility for usage in the calculation of other parameters, as described in the following sub-sections.

TABLE I
List of downloaded parameters.

Parameter	Description	Units
v_{wind_x}	Meridional wind in x direction	m/s
v_{wind_y}	Meridional wind in y direction	m/s
T	Air temperature	K
q	Specific humidity	kg/kg
LWC	Atmospheric cloud condensed water content (Liquid Water Content)	kg/kg

1) Relative Humidity: The specific humidity parameter can be downloaded from the meteorological service. However, in this work, the parameter used in the calculations is not the specific humidity but the relative humidity. This is because the aircraft is assumed to be in icing conditions and turn on the icing protection system when the temperature is below 0 °C and the relative humidity is over 0.99. Therefore, the relative humidity (H) needs to be calculated and it is given by [27]:

$$H(e_a, e_{sat}) = \frac{e_a}{e_{sat}} \tag{20}$$

with the vapour pressure (e_a in [Pa]):

$$e_a(p, q) = \frac{qp}{0.622 + 0.378q} \tag{21}$$

where q is the specific humidity, p is the pressure in [Pa] given by Eq. 1 and with the saturated water vapour pressure (e_{sat} in [Pa]):

$$e_{sat}(T) = 10^{\frac{0.7859 + 0.03477(T - 273.16)}{(1 + 0.00412(T - 273.16))}} + 2 \tag{22}$$

where T is the temperature in [K].

2) LWC and MVD: The "mass fraction of cloud condensed water in air" can be also referred as "liquid water content (LWC)". In the icing protection system regression model, the LWC is one of the input parameters to estimate how much power is required by the system. The regression model uses the LWC concentration in [gm^{-3}] but the downloaded parameter is the LWC mixing ratio in [kg/kg]. Therefore, to convert LWC mixing ratio (LWC_m in [kg/kg]) to LWC concentration (LWC_c in [gm^{-3}]), the gas law for dry air is used:

$$LWC_c(p, LWC_m, T) = \frac{LWC_m p}{R_d T} \times 10^3, \tag{23}$$

where T is the temperature in [K], R_d is the specific gas constant for dry air of 287.058 $Jkg^{-1}K^{-1}$. and p is the pressure in [Pa] given by Eq. 1.

The Water Droplet Median Volume Diameter (MVD in [μm]) is another parameter used to calculate the power required by the icing protection system. It is approximated by following [28] and given by:

$$MVD(\lambda) = \frac{3.672 + \mu}{\lambda}, \tag{24}$$

with the shape parameter (μ) given by:

$$\mu = min\left(\frac{1000}{N_c} + 2,15\right), \tag{25}$$

where N_c is the pre-specified droplet number of 100 cm^{-3} and with:

$$\lambda(LWC_c) = \left[\frac{\pi}{6}\frac{\rho_w N_c}{LWC_c}\frac{\Gamma(\mu+4)}{\Gamma(\mu+1)}\right]^{\frac{1}{3}}, \tag{26}$$

where Γ is the gamma function, ρ_w is the density of water of 1 gm^{-3} and N_c is equal to 100x10^{-6} m^{-3}.

3) Meteorological data download: The Norwegian Meteorological Institute hosts a webapp called THREDDS Data Server, where it is possible to have access to weather forecasts of several meteorological parameters. One of the services is the MetCoOp Ensemble Prediction System (MEPS) [29], from where the parameters used in this work were downloaded. This service provides data for the Scandinavian region with horizontal resolution of 2.5 km and from around 0.00986 to 0.99851 atm pressure levels (that can be converted to altitude) divided into 65 not equally spaced values. In the MEPS service, raw and post processed data are available for 10 ensemble members (set of forecast simulations) and for up to 66 hours of forecast. The models are run every 6 hours (00,06,12,18 UTC) and the first data file (00) is the most complete one and the only file containing all the necessary parameters for the development of this work. Therefore, the 00 file was downloaded for the esemble member 0 (mbr0) and the data from the forecast time slot 0 was used in the simulations. The time slot 0 reflects the instant information of the chosen date/time while the other time slots are hourly forecast.

The files are available in the Network Common Data Form (NetCFD) format and each file is up to 200 GB. However, it is possible to select which parts to download by using the Open-source Project for a Network Data Access Protocol (OPeNDAP). Therefore, the selected parameters can be downloaded only for the region of interest and for the desired pressure levels (altitudes).

B. Elevation data

The elevation data was downloaded from the Norwegian national website for map data (geonorge.no). Geonorge provides a catalog with a wide variety of map products, including elevation maps. These elevation maps are in the form of Digital Terrain Model (DTM) or Digital Surface Model (DSM) and can be visualized in the website or downloaded via WCS or WMS services. In this work, the DTM was used, which is available with 1 m and 15 m of vertical resolution for the regions correspondent to UTM32, UTM33 and UTM35.

1) Elevation data download: To download the data with the WCS service, the web browser can be used as the WCS client. Therefore, the data is requested via HTTP through URL parameters. The commands to be used are: GetCapabilities; DescribeCoverage; and GetCoverage. The first one returns all service-level metadata and a brief description, the second one returns the full description and the third one returns the data itself. The URL parameters varies according to the product and are usually described in the information obtained by the GetCapabilities and DescribeCoverage commands. One of the parameters is regarding horizontal resolution, which in this work, was chosen to be 50 m.

V. Path Planning

The goal of this work is to find a three dimensions path that minimizes the energy consumption of a long range sUAS flight from an origin to a destination in adverse weather conditions. To solve this problem, an optimization technique is used to minimize the given cost function by finding a sub-optimal set of waypoints and airspeed changes.

A. Optimization technique

Since the main goal of this work is to investigate the benefits of integrating the previously described models in the cost function, an optimization technique of simple implementation that is also able to minimize non-convex and discontinuous functions was chosen. Particle Swarm Optimization (PSO) [30] technique is a meta-heuristic optimization method where the particles (solutions) are updated every iteration based on the best global and local solutions. In this study, the standard PSO was used with a modification to reduce the maximum absolute particle velocity by an ϵ factor. This was implemented to keep the search more local, and thereby avoiding too large movements in the solution domain per iteration, as it may be expected that the optimum solution is relatively close to the straight line path.

The parameters that must be defined in the PSO algorithm are: the number of iterations, which was chosen as 400; the cognitive and social parameter (c_1 and c_2, respectively) which were chosen both as 2.0; and the velocity constraint factor (ϵ), which was chosen as 0.1.

In addition, the boundaries of the variables (minimum and maximum airspeed and climb angle) must also be defined according to the aircraft platform, as well as to the mission envelope, in order to limit the search to the region where the solution is certain to be.

It is important to address that other meta-heuristic optimization techniques may also be applied to this problem, achieving similar results.

B. Optimization algorithm

The algorithm's block diagram is shown in Fig. 5. The orange blocks scenario-based input parameters, such as the

meteorological and elevation data, the origin and destination, the number of decision variables and the PSO parameters. The other boxes outside the blue box are part of the pre-processing phase when the model is created and the initial solutions are generated.

The blue box contains the optimization loop. First the candidate solutions are evaluated with respect to the terrain. If part of the path is under terrain, the solution is discarded ($cost = \infty$). If not, the optimization will evaluate the icing conditions for each discretization step i.

If icing conditions are present in the step i ($H_i > 99\%$ and $T_i < 0$ °C), the deice and anti-ice required power are calculated (P_{deice_i} and $P_{anti-ice_i}$, respectively). For the deicing operations the engine's required power is calculated with an updated drag coefficient ($C^*_{D_i}$), which constitutes the average icing penalty, and therefore an updated required propulsive power $P^*_{shaft_i}$. For the anti-ice operations the aircraft's wings are kept clear from icing. Therefore the engine's required power is the same as without ice (P_{shaft_i}). However, the anti-icing system does require thermal energy. In this study the anti-icing system uses the main battery as power source (i.e. does not have a separate power source), and therefore induces a performance penalty during usage. The total power required by the deice and anti-ice systems, including the respective engine's required power, are compared and the solution that requires the least total power is chosen. If there are no icing conditions present the total required propulsion power remains unchanged (P_{shaft_i}).

The next step is to calculate the battery energy consumption in the step i taking into consideration the battery model and how much battery capacity is left. Finally, the total battery energy consumption is calculated by summing the battery energy consumption times the flight time of all steps. The total battery energy consumption is, therefore, used to update the particles' position in the domain. The new solutions are then evaluated. This process repeats for the chosen total number of iterations.

C. Cost Function

The aim of the optimization algorithm is to minimize a cost function (Eq. 27), which represents the total energy consumption and is calculated by the sum of the battery discharge rate ($\dot{C}$ in [Ah/s]) in each discretization step, multiplied by the time in each discretization step:

$$minimize\, C_{tot}(\dot{\mathbf{C}}, \mathbf{t}) = \sum_{i=1}^{N} \dot{C}_i t_i \tag{27}$$

where $\dot{\mathbf{C}}$ and $\mathbf{t}$ are the vectors with all $\dot{C}_i$ and t_i, respectively. C_{tot} is the total discharged capacity in [Ah], i is the index of the discretization step, N is the number of discretization steps in the path, t_i is the time in [s] at the i-th step given by:

$$t_i(L_{step}, v_{gs_i}) = L_{step}/v_{gs_i}, \tag{28}$$

where v_{gs_i} is the ground speed in the discretization step i in [m/s] given by Eq. 11, with the step's length (L_{step} in [m]) given by:

$$L_{step}(L) = \frac{L}{N}, \tag{29}$$

and with the total length of the path (L in [m]) given by:

$$L(\mathbf{x}, \mathbf{y}) = \sum_{i=1}^{N} \sqrt{(x_{i+1} - x_i)^2 + (y_{i+1} - y_i)^2} \tag{30}$$

where x_i and y_i are east and north positions in the ENU frame and i is the index of the discretization step.

The the rate of discharge ($\dot{C}$ in [Ah/s]) given by:

$$\dot{C}_i(I_{tot_i}) = \frac{I_{tot_i}}{3600}, \tag{31}$$

with the total current (I_{tot} in [A]) given by:

$$I_{tot_i}(P_{tot_i}, V_{oc_i}) = \frac{P_{tot_i}}{V_{oc_i}}, \tag{32}$$

where V_{oc} is the battery's potential in [V] (Eq. 19) and with the total required power (P_{tot} in [W]) given by:

$$P_{tot}(P_{shaft}) = P_{shaft}, \tag{33}$$

if there are not icing conditions occurring, or

$$P_{tot}(P^*_{shaft}, P_{deice}) = P^*_{shaft} + P_{deice}, \tag{34}$$

when there are icing conditions occuring, and the deice solution is the one requiring the least power, or

$$P_{tot}(P_{shaft}, P_{anti-ice}) = P_{shaft} + P_{anti-ice} \tag{35}$$

if there are icing conditions, while the anti-ice solution requires the least power. Here, P_{shaft} is the engine's required power in [W] (Eq. 6), P^*_{shaft} is the engine's required power when using the deice solution in [W] (Eq. 40), $P_{anti-ice}$ is the anti-ice solution required power in [W] and P_{deice} is the deice solution required power in [W].

Finally, C_i is the total capacity discharged in [Ah] until instant i and given by:

$$C_i(\dot{\mathbf{C}}_i, \mathbf{t}_i) = \sum_{i=0}^{i} \dot{C}_i t_i, \tag{36}$$

where $\dot{\mathbf{C}}_i$ is the vector of $\dot{C}$ from $\dot{C}_0$ to $\dot{C}_i$ and $\mathbf{t}_i$ is the vector of t from t_0 to t_i. C_0 is the initial discharged capacity.

Note that when parts of the path are not above the terrain, or if the total energy consumption is higher than the battery's capacity, this candidate solution receives an infinite penalty to ensure it is disregarded as a candidate solution.

D. Decision variables

The required decision variables are horizontal plane waypoints (x,y), airspeeds (v_a) and climb angles (θ). The number of waypoints (O) and airspeeds/climb angles (K) are chosen by the user when defining the scenario. Note that the airspeed and climb angle changes were chosen to occur at the same time for algorithm simplicity.

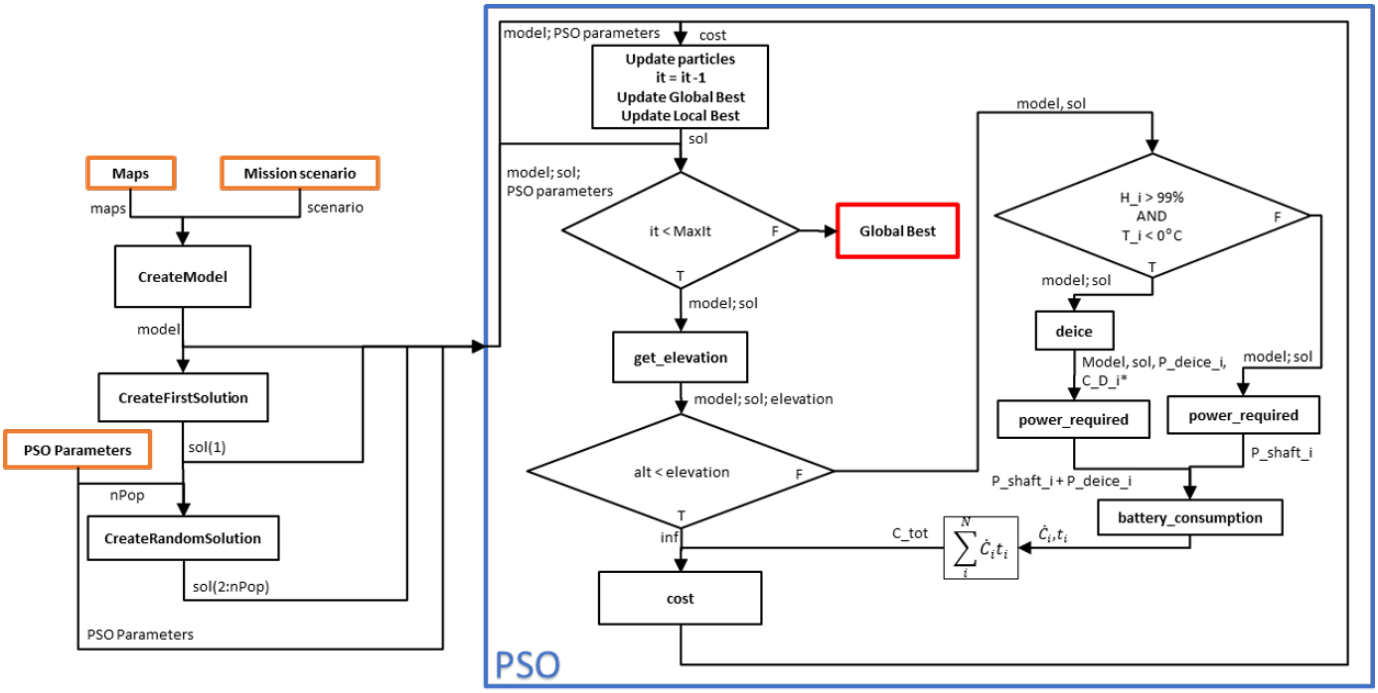

Fig. 5. Algorithm block diagram.

E. Model and Mission Parameters

1) ENU frame: The ENU frame was chosen as the coordinate system of the optimization algorithm. Therefore, all information in World Geodetic System 1984 (WGS84), which is in the format of latitude, longitude and altitude, must be converted to the ENU frame. Also, the resulting waypoints of the optimized solution must be converted to WGS84 in order to be fed into the sUAS' flight control system.

In this work, when using the ENU frame, the x axis points east, the y axis points north and the z axis points up.

It is also necessary to define the origin (0,0,0) of the ENU frame. As the region around the origin is less affected by the frame conversion error, the origin was chosen to be in the geographical midpoint between origin and destination at sea level.

2) Domain: The candidate solutions' waypoints are limited to be away from the straight path up to a maximum distance. This maximum distance was defined as one third of the length of the straight path between the origin and destination. Therefore, the optimization algorithm can only find candidate solutions containing waypoints within this domain region.

The boundaries of airspeed (v_a) and climbing angle (θ) must also be defined according to the aircraft platform's constraints. In addition, these boundaries should be fine tuned for values around the expected optimization resulting values, in order to achieve faster convergence.

3) Discretization strategy: The cost function (Eq. 27) is evaluated for each discretization step of the path and the total cost is the sum of the energy consumption in each step. Therefore the number of steps will affect the resolution of the optimization algorithm, and the processing time. The number of discretization steps (N) is defined by the multiplication factor (F) and the number of airspeed and climb angle changes (K):

$$N = KF - 1 \tag{37}$$

These parameters are presented for a scenario example in Fig. 6. In this example, A is the origin and B is the destination. There is one waypoint between origin and destination ($O = 1$). There are three airspeed and climb angle changes ($K = 3$), and three of multiplication factor ($F = 3$). Therefore there are eight discretization steps (N).

Increasing the number of discretization steps makes the optimization more accurate. However, the computation time is increased accordingly. The lower limit of the distance between discretization steps that could affect the results is the lowest resolution step of the data used. In the case of this work, that is the resolution of 50 m of terrain elevation.

It is also relevant to note that after the optimization and before the flight, it is important to make an evaluation of the path regarding the terrain elevation with a low resolution step, in order to make sure that the entire length of the path is above the terrain.

Additionally, the first particle in the PSO algorithm has to be initiated with a candidate solution. A good candidate initial solution for the first particle is a straight path from origin to destination, climbing with constant climb angle to the altitude a few meters above the highest peak, then cruising close to the destination, and finally descending with constant negative climb rate to the destination.

Also, the other particles (candidate solutions) of the population must be initiated. To not distract the optimization algorithm from the region around the first candidate solution, which is expected to contain an optimal solution, the particles

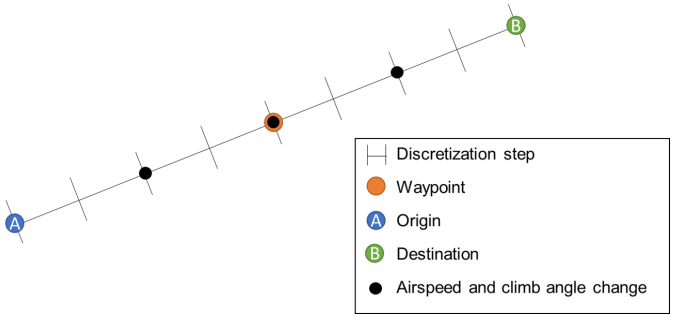

Fig. 6. Example of a path and its division.

are chosen to be variations of the first particle following the exponential probability distribution. Therefore, the values of the set of variables of the other particles are close to the values of the first initial solution set of variables.

VI. Case Study

In this section, the chosen mission case and operational profiles that were evaluated are described, and the aircraft and battery parameters used in the optimization algorithm are explained.

A. Aircraft platform

The P31016 (Fig. 7) is a small battery-powered aircraft that is powered by a 6.0 kilowatt brushless motor. The propulsion efficiency (η_p) is assumed constant at 50% with an ideal electrical discharge pattern. This value lies in range of typical typical propulsion efficiency of a small UAS, as described in [31] The aircraft has a wing surface (S) of 0.81 m^2 and has a typical mission-ready weight of 171.5 N (W).

Fig. 7. P31016 concept battery-powered fixed-wing unmanned aircraft

Due to factory specification, the climb angle (θ) was set ranging from -10 to 10 degrees. Regarding the airspeed (v_a), it was set ranging from 20 m/s to 30 m/s. This choice was made to avoid the optimization algorithm explores too high airspeed, considering the aircraft performance and mission envelope.

The aircraft performance data was generated with the flow solving module FENSAP, which is part of FENSAP-ICE [32]. Three-dimensional CFD simulations were performed on the P31016 (Fig. 7) at Reynolds number (Re) of 1.2×10^6 with angles of attack (AOA) corresponding to the set envelope limitations and using a numerical setup described in Table III. The results for drag and lift of the P31016 are presented in Fig. 8. The simulations indicate that the flow separation starts from the trailing-edge at AOA of 8 deg. Drag forces increase unproportionally after the onset of stall, whereas lift is decreased as the separation intensifies with higher AOAs.

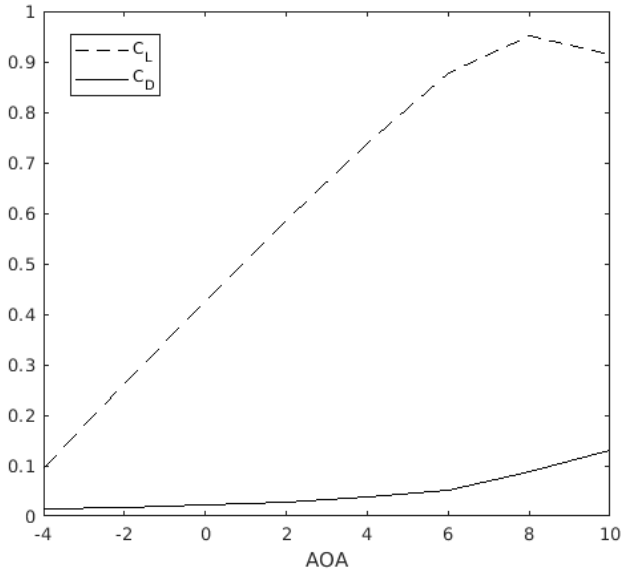

Fig. 8. AOA (Angle-Of-Attack) vs C_D and C_L from CFD simulations

This data was used to fit the drag polar curve (Fig. 9). The curve was fitted for a lift coefficient range calculated based on the aircraft and mission constrains. These constrains are: minimum and maximum airspeed (v_a), minimum and maximum climb angle (θ) and minimum and maximum air density (ρ). The air density was calculated according to the minimum and maximum expected relative humidity (H), temperature (T) and pressure (p) in the meteorological data. The minimum and maximum resulting lift coefficient for these constrains were 0.3436 and 1.0371 respectively. The fitted curve of the drag polar for this range is given as:

$$C_D(C_L) = 0.1407C_L^2 - 0.07989C_L + 0.02496, \qquad (38)$$

where C_L is the lift coefficient and C_D is the drag coefficient.

B. Icing protection System model

The power requirements for de-icing and anti-icing, as well as the performance penalties during de-icing are generated using numerical simulation methods. Two icing codes are used for this. LEWICE is an icing code that has been developed by NASA over several decades for general aviation [33]. It is a widely validated code [34], but it has been shown that there may be limitations for the application of sUAS [35] [36]. The code is based on a panel-method, that can simulate ice accumulation, anti-icing, and de-icing with very low computational resources. ANSYS FENSAP-ICE is an icing code using modern computational fluid dynamics (CFD)

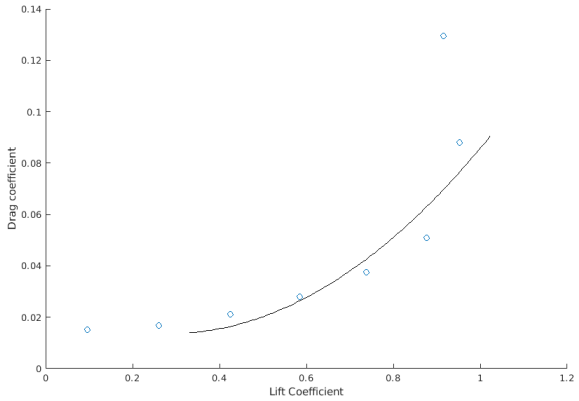

Fig. 9. Drag polar fitted curve

methods [37]. The code is very flexible and has in the past been used for UAS applications [38] but still lacks a dedicated validation for icing at small Reynolds numbers [39].

In this work, the LEWICE is used to generate a model for the anti-icing and de-icing loads, whereas FENSAP-ICE is used for the de-icing performance penalties. The low computational requirements of the panel-method of LEWICE allow to simulate a large number of different meteorological icing conditions in short time, in the order of minutes on a typical desktop computer. The same computations would take several days on a high-performance computing (HPC) cluster with FENSAP-ICE.

A total of 112 different icing cases have been simulated with LEWICE to generate a dataset for anti-icing with LEWICE. The boundary conditions of the meteorological cases are based on the icing envelope of 14 CFR Part 25, App. C [40] used for the airworthiness certification of commercial aircrafts. The simulation cases cover the intermittent maximum (IM) icing and continuous maximum (CM) icing envelope. The range of values for each icing parameter is shown in Table II. Simulations were performed in 2D using the mean aerodynamic chord (MAC = 0.275 m) of the wing. For all simulation it was assumed that only 20% of the leading-edge area of the lifting surfaces was protected (surface temperature of +5 °C). Runback icing, generated by the refreezing of melted ice from the heated zones, was not included in this study. This was done for reasons of simplification and lack of dedicated studies of runback icing on sUAS. Runback icing itself may be a significant source of aerodynamic performance degradation of any IPS [41].

TABLE II
RANGE OF VALUES FOR EACH ICING PARAMETER

Parameter	Range of values
Airspeed	[20, 30, 40, 50] m/s
Angle of attack AOA	[0] deg
Chord c	[0.275] m
Temperature T_C	[-2, -5, -10, -30] °C
Median (droplet) volume diameter MVD	[15, 20, 30, 40] μm
Liquid water content LWC concentration	[0.04 ... 2.82] gm^{-3}

The de-icing power requirements have been assumed to be 60% lower than the anti-icing loads. In contrast to the anti-icing, the minimum power requirement for de-icing can not be directly simulated with a steady-state assumption. This means that transient simulations that prescribe a power supply to the leading-edge is required. Such simulations were carried out with LEWICE and confirmed that the aforementioned assumption provides sufficient power for successful de-icing. It should be noted however, that this assumption is a gross simplification, but is deemed sufficient for the purpose of this work.

The 112 simulation cases from LEWICE for the anti-icing and de-icing power requirements ($P_{anti-ice}$ and P_{deice}, respectively) were used to generate linear models that are used for the path-planning optimization. Forth order linear regression models were used and have been found to be able to predict the power loads depending on airspeed (v_a in [m/s]), temperature (T_C in [°C]), Liquid Water Content concentration (LWC_c in gm^{-3}) and Median Volume Diameter (MVD in [μm]) with good accuracy (R^2= 0.977).

The data for the de-icing performance degradation was obtained with FENSAP-ICE in 2D and then extrapolated for the entire aircraft. First, 90 s of ice accretion were simulated with FENSAP-ICE with the numerical parameters specified in Table III. The degradation of lift and drag was then averaged over a full de-icing cycle of 120 s. Again the 14 CFR Part 25, App. C icing envelopes (CM & IM) were applied. In order to reduce the number of simulations, only the cruise velocity of 25 m/s and a single MVD of 20 μm was considered.

TABLE III
NUMERICAL PARAMETERS SETUP

Parameter	Setup
Flow conditions	Steady-state, fully turbulent
Turbulence model	Spalart-Allmaras
Droplet distribution	Monodisperse
Artificial	Second order
Viscosity	Streamline upwind

The aerodynamic degradation occurring during de-icing is presented in Fig. 10 and 11. A linear model (Eq. 39) was selected for the drag (R^2 = 0.81).

$$C_D^*(C_D, LWC_c) = C_D + C_D(0.0785 LWC_c + 0.4973). \quad (39)$$

Therefore, the required power to propel the aircraft when the de-icing solution is used (P^*_{pshaft} in [W]) needs to be calculated using the degraded drag coefficient (C_D^*):

$$P^*_{pshaft}(\rho, v_a, C_D^*, \theta) = \frac{(0.5\rho v_a^2 S C_D^* + W sin(\theta))v_a}{\eta_p}. \quad (40)$$

1) Battery parameters: The P31016 is assumed to be equipped with a commercial 10-cells LiPo battery with 26.4 Ah capacity (C_{cut}). Following Tremblay's model, the potential parameters of a 10-cells LiPo battery are approximately: 41.8, 39.67 and 37.67 ampere-hour of fully charged (V_{full}), end of exponential range (V_{exp}) and end of nominal range (V_{nom}) respectively. The capacity parameters are approximately: 2.64 and 20.4 ampere-hour of end of exponential range (C_{exp}) and

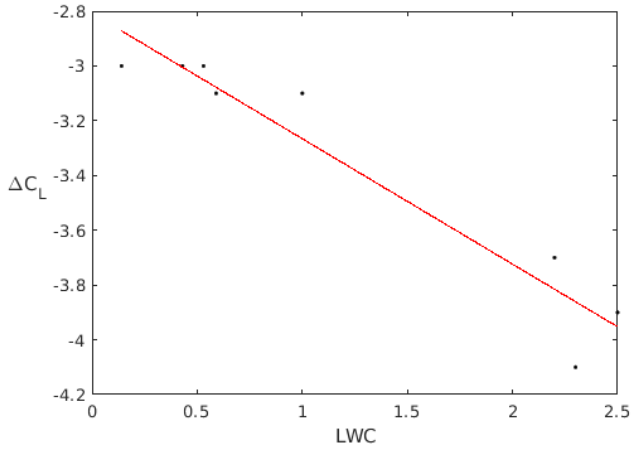

Fig. 10. LWC [gm^{-3}] vs ΔC_L [%] degradation

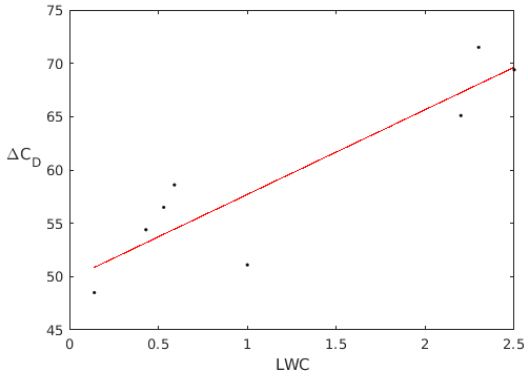

Fig. 11. LWC [gm^{-3}] vs ΔC_D [%] degradation

end of nominal range (C_{nom}), respectively. In addition, from the battery's manual it is found that the internal resistance (R_c) is 0.015 Ohms and the maximum rated discharge current (I_{rated}) to be 660 ampere. The potential curve of this battery with respect to the capacity discharged for 10 ampere of constant current is shown in Fig. 12.

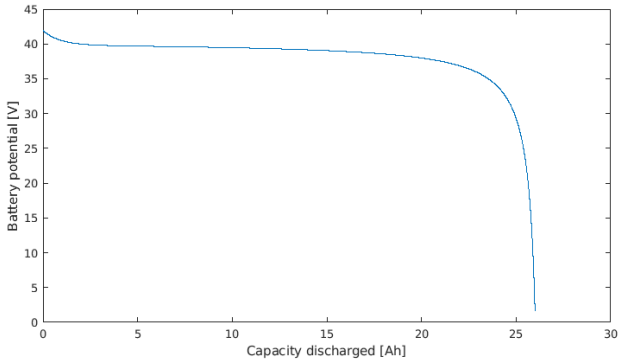

Fig. 12. Battery potential times capacity discharged

Note that for all cases, the battery was assumed to be fully charged in the beginning of the mission. Therefore, C_0 (the initial capacity discharged of the battery) was assumed to be equal to 0 Ah.

C. Mission Case

The region of Northern Norway was chosen for the evaluation of the proposed solution. The meteorological and elevation data were obtained for the area of the white rectangle of Fig. 14. In this area, one mission case was defined to be investigated and the weather of the date of 20th of January of 2019 was chosen as the reference weather. For this area and date, the parameters of liquid water content concentration (LWC_c in [gm^{-3}]) and temperature in °C are related as shown in Fig. 13 if icing conditions are met.

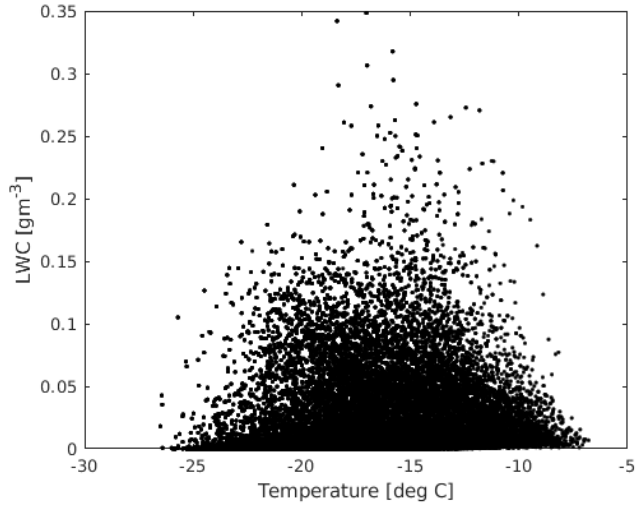

Fig. 13. LWC_c and temperature distribution.

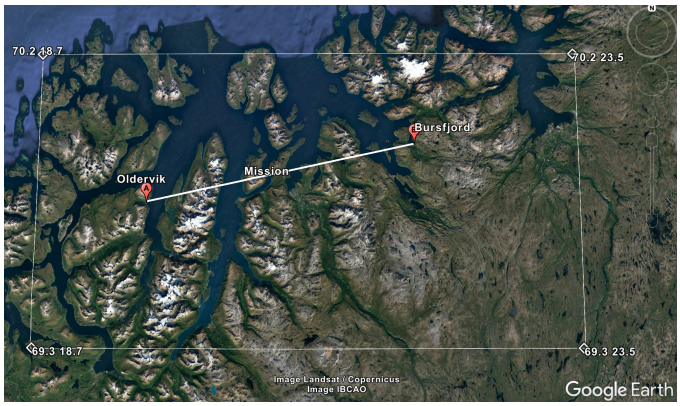

Fig. 14. Mission case.

1) Operational Profiles: For the mission case, twelve different operational profiles (OP) were evaluated as described below.

Note that all the operational profiles start at 250 m of altitude, regardless of the altitude of the take off spot. Therefore, it is assumed that before starting the autopilot, the aircraft will be taken by the pilot to 250 m of altitude. Also, when reaching the destination, the aircraft must be landed by the pilot. Take off and landing maneuvers are not considered in this work.

The straight paths are assumed to have constant airspeed of 28 m/s, which is around the value of the best cruise airspeed for the P31016.

- OP 01: Horizontal straight path between origin and destination, climbing to a few meters above the highest peak, flying at constant altitude until close to the destination, then descending until the destination. Evaluated under no icing conditions.
- OP 02: Optimized path without considering icing conditions. Evaluated under no icing conditions.
- OP 03: Optimized path considering icing conditions, using deice or anti-ice (best option) when needed. Evaluated under no icing conditions.
- OP 04: Optimized path considering icing conditions, using only anti-ice when needed. Evaluated under no icing conditions.
- OP 05: Horizontal straight path between origin and destination, climbing to a few meters above the highest peak, flying at constant altitude until close to the destination, then descending until the destination. Evaluated under icing conditions, using deice or anti-ice (best option) when needed.
- OP 06: Optimized path without considering icing conditions. Evaluated under icing conditions, using deice or anti-ice (best option) when needed.
- OP 07: Optimized path considering icing conditions, using deice or anti-ice (best option) when needed. Evaluated under icing conditions, using deice or anti-ice (best option) when needed.
- OP 08: Optimized path without considering icing conditions. Evaluated under icing conditions, using only anti-ice when needed.
- OP 09: Horizontal straight path between origin and destination, climbing to a few meters above the highest peak, flying at constant altitude until close to the destination, then descending until the destination. Evaluated under icing conditions, using only anti-ice when needed.
- OP 10: Optimized path considering icing conditions, using only anti-ice when needed. Evaluated under icing conditions, using deice or anti-ice (best option) when needed.
- OP 11: Optimized path considering icing conditions, using only anti-ice when needed. Evaluated under icing conditions, using only anti-ice when needed.
- OP 12: Optimized path considering icing conditions, using deice or anti-ice (best option) when needed. Evaluated under icing conditions, using only anti-ice when needed.

2) Discretization: The number of waypoints (O) was defined as 5; the number of airspeed and climb angle changes (K) as 20; and the multiplication factor (F) as 5, giving a total of 99 discretization steps (N). Since the straight path has around 90 km, this gives a discretization step length of around 1 km.

VII. Results

Table IV show the results for the mission case, where the sUAS flies from Oldervik to Bursfjord. In icing conditions, the operational profile seven has the lowest battery energy consumption (7.05 Ah), as expected. Compared to the operational profile one, which consumes 14.82 Ah of battery, it brings a reduction of 52.43 % on the battery energy consumption. Also, in this mission case, if only the anti-ice is used and the sUAS is flying straight (OP 09), the battery energy consumption is equal to 20.54 Ah, almost three times more than the optimized path that both deice and anti-ice are available. This is due to the absence of path optimization and to the fact that the anti-ice system requires more power.

In addition, if the path is optimized without taking the ice into consideration, the expected battery energy consumption is of 6.28 Ah (OP 02). However, if the sUAS actually experiences icing conditions during this flight, the battery energy consumption is of 10.74 Ah (OP 06), against 7.05 Ah when the path is optimized taking into consideration the weather forecast (OP 07). Therefore, this shows the importance of using the weather information to optimize the path.

All optimized paths were longer than the straight path. Also, the flight time was slightly longer in all cases. This is due to the fact the optimization takes the wind into consideration so it is able to change the path to find a better wind profile and/or to change the airspeed accordingly. Therefore, the flight duration is longer but the battery energy consumption is lower.

Figure 15 shows the straight path (OP 05) and Fig. 16 the optimized path (OP 07) of the mission case. It is possible to notice that in the optimization, the path is optimized so that the ice is avoided when possible by placing it under or above the icing clouds (blue dots). Also, when close to the destination, the descent maneuver is started as soon as possible, so energy savings are enhanced.

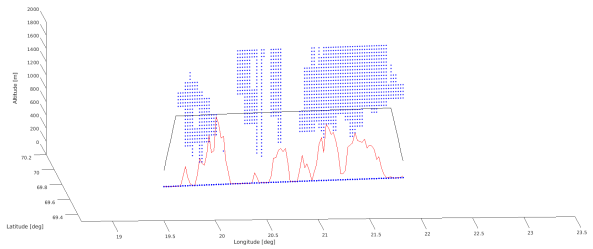

Fig. 15. Straight path.

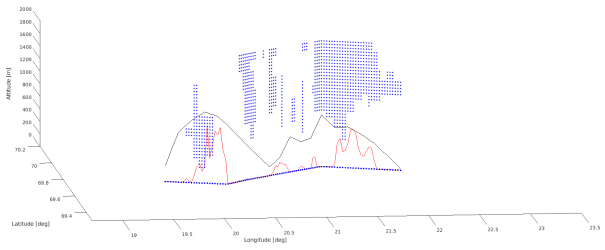

Fig. 16. Optimized path.

The two peaks on the battery consumption (Fig. 17) between 5 and 10 minutes and between 35 and 40 minutes are due to the icing conditions. In the first moment that the sUAS is flying under icing conditions, the power required by the deice

TABLE IV
MISSION CASE OPERATIONAL PROFILES RESULTS

	Straight	Opt. without ice	Opt. with anti-ice	Opt. with deice	Eval. with anti-ice	Eval. with deice	Battery Cons. [Ah]	Length [km]	Time [min]	Length in ice [km]	Time in ice [min]
OP 01	x						8.08	91.47	44.68	0.00	0.00
OP 02		x					6.28	91.82	45.59	0.00	0.00
OP 03			x	x			6.52	97.49	49.80	0.00	0.00
OP 04			x				6.65	94.84	50.36	0.00	0.00
OP 05	x				x	x	14.82	91.47	44.68	49.39	23.32
OP 06		x			x	x	10.74	91.82	45.59	34.89	16.27
OP 07			x	x	x	x	7.05	97.49	49.80	3.90	1.96
OP 08		x			x		14.32	91.82	45.59	34.89	16.27
OP 09	x				x		20.54	91.47	44.68	49.39	23.32
OP 10			x		x	x	7.09	94.84	50.36	3.79	1.71
OP 11			x		x		7.46	94.84	50.36	3.79	1.71
OP 12			x	x	x		7.48	97.49	49.80	3.90	1.96

system is 477 W and the increase on the power required to propel the aircraft is 184 W, totalizing 661 W. The increase on the propulsion required power is due to the drag coefficient penalty brought by the deice system. If the anti-ice solution was used, where there is no penalty on the drag, the required power would be around 1150 W. Therefore, the deice solution requires less power in total (deice system plus propulsion power). The predominance of the deice solution over the anti-ice will repeat in almost every case investigated in this work. This is due to the mission constrains and to the fact that, according to the deice and anti-ice regression models used in this work, the anti-ice will only have an advantage in maneuvers with high drag.

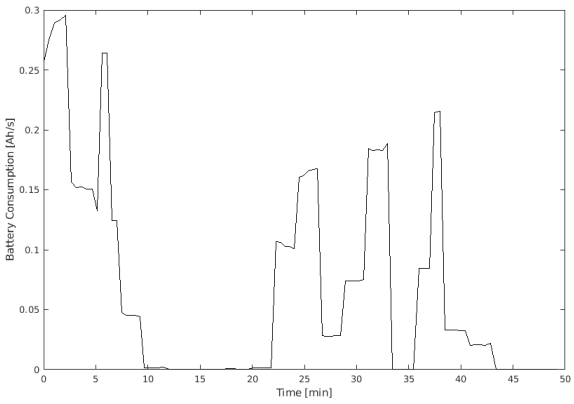

Fig. 17. Battery Consumption.

Finally, Fig. 19 shows the optimized airspeed along the path (OP 07). It is possible to notice that the airspeed is kept around the known best cruise airspeed of the aircraft, which is around 28 m/s.

It should be noted that several simplifications have been applied to some of the simulation input of this study regarding the icing protection system and icing effects that may have a significant influence on the overall results:

- No runback icing effects
- Simplified de-icing load calculation
- Simplified simulation of the aerodynamic degradation during de-icing

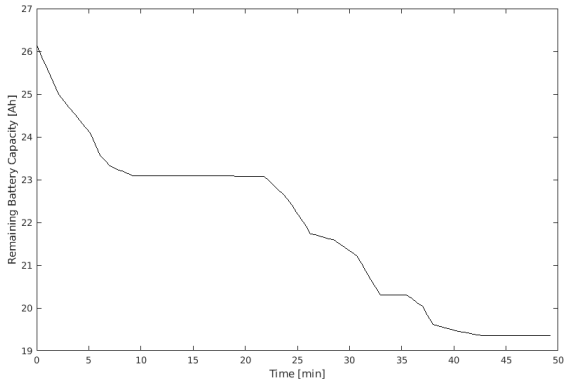

Fig. 18. Battery Discharged.

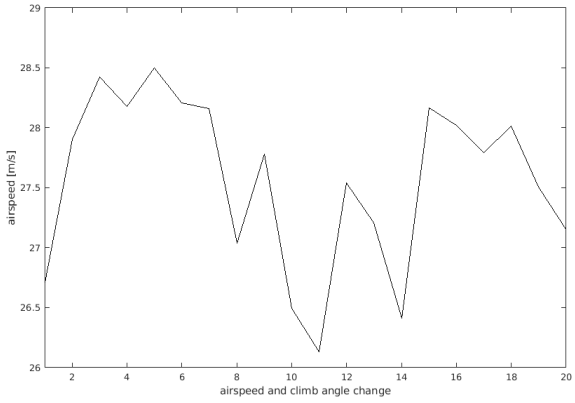

Fig. 19. Airspeed of optimized path.

These simplifications were introduced in order to limit the amount of expensive computational simulations. Since this work is focussing mostly on the path-planning method, these simplifications were considered sufficient for this study. For future work, a greater level of detail can easily be included to the required input data.

VIII. Conclusion

This work presented a path-planning algorithm for sUAS equipped with icing protection systems. An aircraft performance model was used to calculate the power required to propel the aircraft. A battery model was also included in the calculations to give a more precise battery consumption. The goal of the algorithm was to find an optimum path that uses the least energy, taking into consideration the atmospheric parameters, such as wind, liquid water content, relative humidity and temperature of a given time. Climb/decent angles, airspeed and waypoints were the optimization variables. The investigated mission case was to fly between two towns in Northern Norway in a given date of the winter season. Twelve operational profiles were compared and the proposed solution, that takes the icing conditions into consideration when optimizing the path, achieved 52% of battery savings when compared to the standard straight path, proving itself to be a very useful solution for path-planning in icing conditions. In addition, it was verified that, for the sUAS used in this work, the deice solution will require less power to protect the sUAS from icing in the majority of situations, compared to the anti-ice solution.

Acknowledgment

This work has been carried out at the Centre for Autonomous Marine Operations and Systems (AMOS), supported by the Research Council of Norway through the Centres of Excellence funding scheme, project number 223254. This project has received funding from the European Union's Horizon 2020 research and innovation programme under the Marie Sklodowska-Curie grant agreement No 642153. We would also like to acknowledge Research Council of Norway and industry partners for funding through projects: CIRFA 237906; and RFFMN D-ICE 285248. The CFD computations were performed on resources provided by UNINETT Sigma2 - the National Infrastructure for High Performance Computing and Data Storage in Norway. We also want to acknowledge Mr. Øyvind Byrkjedal from Kjeller Vindteknikk for the help with LCW and MVD calculations.

References

[1] Z. He and L. Zhao, "The comparison of four uav path planning algorithms based on geometry search algorithm," in *2017 9th International Conference on Intelligent Human-Machine Systems and Cybernetics (IHMSC)*, vol. 2. IEEE, 2017, pp. 33–36.

[2] P. Chandler, S. Rasmussen, and M. Pachter, "Uav cooperative path planning," in *AIAA Guidance, Navigation, and Control Conference and Exhibit*, 2000, pp. 1255–1265.

[3] K. Yang and S. Sukkarieh, "3d smooth path planning for a uav in cluttered natural environments," in *Intelligent Robots and Systems, 2008. IROS 2008. IEEE/RSJ International Conference on*. IEEE, 2008, pp. 794–800.

[4] I. K. Nikolos, K. P. Valavanis, N. C. Tsourveloudis, and A. N. Kostaras, "Evolutionary algorithm based offline/online path planner for uav navigation," *IEEE Transactions on Systems, Man, and Cybernetics, Part B (Cybernetics)*, vol. 33, no. 6, pp. 898–912, 2003.

[5] A. Richards and J. P. How, "Aircraft trajectory planning with collision avoidance using mixed integer linear programming," in *American Control Conference, 2002. Proceedings of the 2002*, vol. 3. IEEE, 2002, pp. 1936–1941.

[6] S. Li, X. Sun, and Y. Xu, "Particle swarm optimization for route planning of unmanned aerial vehicles," in *Information Acquisition, 2006 IEEE International Conference on*. IEEE, 2006, pp. 1213–1218.

[7] R. Beard and T. McLain, *Small Unmanned Aircraft: Theory and Practice*. Princeton University Press, 2012.

[8] A. Rucco, A. P. Aguiar, and F. L. Pereira, "A predictive path-following approach for fixed-wing unmanned aerial vehicles in presence of wind disturbances," *Robot 2015: Second Iberian Robotics Conference*, vol. 8, pp. 623–634, 2016.

[9] W. H. Al-Sabban, L. F. Gonzalez, and R. N. Smith, "Wind-energy based path planning for unmanned aerial vehicles using markov decision processes," in *Robotics and Automation (ICRA), 2013 IEEE International Conference on*. IEEE, 2013, pp. 784–789.

[10] A. L. Jennings, R. Ordonez, and N. Ceccarelli, "An ant colony optimization using training data applied to uav way point path planning in wind," in *Swarm Intelligence Symposium, 2008. SIS 2008. IEEE*. IEEE, 2008, pp. 1–8.

[11] M. Coombes, W.-H. Chen, and P. Render, "Landing site reachability in a forced landing of unmanned aircraft in wind," *Journal of Aircraft*, vol. 54, pp. 1415–1427, 2017.

[12] A. R. Hovenburg, F. A. de Alcantara Andrade, C. D. Rodin, T. A. Johansen, and R. Storvold, "Contingency path planning for hybrid-electric uas," in *2017 Workshop on Research, Education and Development of Unmanned Aerial Systems (RED-UAS)*. IEEE, 2017, pp. 37–42.

[13] ——, "Inclusion of horizontal wind maps in path planning optimization of uas," in *2018 International Conference on Unmanned Aircraft Systems (ICUAS)*. IEEE, 2018, pp. 513–520.

[14] M. B. Bragg, A. P. Broeren, and L. A. Blumenthal, "Iced-airfoil aerodynamics," *Progress in Aerospace Sciences*, vol. 41, no. 5, pp. 323–362, 2005.

[15] F. T. Lynch and A. Khodadoust, "Effects of ice accretions on aircraft aerodynamics," *Progress in Aerospace Sciences*, vol. 37, no. 8, pp. 669–767, 2001.

[16] R. Siquig, "Impact of icing on unmanned aerial vehicle (uav) operations," NAVAL ENVIRONMENTAL PREDICTION RESEARCH FACILITY MONTEREY CA, Tech. Rep., 1990.

[17] K. Szilder and S. McIlwain, "In-flight icing of uavs-the influence of reynolds number on the ice accretion process," SAE Technical Paper, Tech. Rep., 2011.

[18] K. Szilder and W. Yuan, "The influence of ice accretion on the aerodynamic performance of a uas airfoil," in *53rd AIAA Aerospace Sciences Meeting*, 2015, p. 0536.

[19] K. L. Sørensen, "Autonomous icing protection solution for small unmanned aircraft: An icing detection, anti-icing and de-icing solution," 2016.

[20] R. Hann, K. Borup, A. Zolich, K. Sorensen, H. Vestad, M. Steinert, and T. Johansen, "Experimental investigations of an icing protection system for uavs," SAE Technical Paper, Tech. Rep., 2019.

[21] Z. Goraj, "An overview of the deicing and anti-icing technologies with prospects for the future," in *24th international congress of the aeronautical sciences*, vol. 29, 2004.

[22] V. Roberge, M. Tarbouchi, and G. Labonté, "Comparison of parallel genetic algorithm and particle swarm optimization for real-time uav path planning," *IEEE Transactions on Industrial Informatics*, vol. 9, no. 1, pp. 132–141, 2013.

[23] I. C. A. Organization, *Manual of the ICAO Standard Atmosphere: Extended to 80 Kilometres (262 500 Feet)*. International Civil Aviation Organization, 1993, vol. 7488.

[24] S. Gudmundsson, "A biomimetic, energy-harvesting, obstacle-avoiding, path-planning algorithm for uavs," Ph.D. dissertation, Embry-Riddle Aeronautical University, 2016.

[25] O. Tremblay, L.-A. Dessaint, and A.-I. Dekkiche, "A generic battery model for the dynamic simulation of hybrid electric vehicles," in *2007 IEEE Vehicle Power and Propulsion Conference*. Ieee, 2007, pp. 284–289.

[26] B. Fuller and E. Mark, "Generic battery rate-effect model," NAVAL UNDERSEA WARFARE CENTER DIV NEWPORT RI AUTONOMOUS AND DEFENSIVE ..., Tech. Rep., 2012.

[27] A. E. Gill, *Atmosphere—ocean dynamics*. Elsevier, 2016.

[28] G. Thompson, B. E. Nygaard, L. Makkonen, and S. Dierer, "Using the weather research and forecasting (wrf) model to predict ground/structural icing," in *13th International Workshop on Atmospheric Icing on Structures, METEOTEST, Andermatt, Switzerland*, 2009.

[29] M. Müller, M. Homleid, K.-I. Ivarsson, M. A. Køltzow, M. Lindskog, K. H. Midtbø, U. Andrae, T. Aspelien, L. Berggren, D. Bjørge *et al.*, "Arome-metcoop: A nordic convective-scale operational weather pre-

diction model," *Weather and Forecasting*, vol. 32, no. 2, pp. 609–627, 2017.
[30] R. Eberhart and J. Kennedy, "A new optimizer using particle swarm theory," in *Micro Machine and Human Science, 1995. MHS'95., Proceedings of the Sixth International Symposium on*. IEEE, 1995, pp. 39–43.
[31] B. Theys, G. Dimitriadis, P. Hendrick, and J. De Schutter, "Influence of propeller configuration on propulsion system efficiency of multi-rotor unmanned aerial vehicles," in *2016 international conference on unmanned aircraft systems (ICUAS)*. IEEE, 2016, pp. 195–201.
[32] ANSYS, "Ansys fensap-ice user manual 18.2," 2017.
[33] W. Wright, "User's manual for lewice version 3.2," 2008.
[34] W. Wright and A. Rutkowski, "Validation results for lewice 2.0" and cd-rom," 1999.
[35] R. Hann, "Uav icing: Comparison of lewice and fensap-ice for ice accretion and performance degradation," in *2018 Atmospheric and Space Environments Conference*, 2018, p. 2861.
[36] ——, "Uav icing: Comparison of lewice and fensap-ice for anti-icing loads," in *AIAA Scitech 2019 Forum*, 2019, p. 1286.
[37] W. G. Habashi, F. Morency, and H. Beaugendre, "Fensap-ice: a comprehensive 3d simulation tool for in-flight icing," in *7th International Congress of Fluid Dynamics and Propulsion, Sharm-El-Sheikh, Egypt, December*, 2001, pp. 1–7.
[38] W. G. Habashi, M. Aubé, G. Baruzzi, F. Morency, P. Tran, and J. C. Narramore, "Fensap-ice: a fully-3d in-flight icing simulation system for aircraft, rotorcraft and uavs," in *24th International Congress of The Aeronautical Sciences*, 2004, pp. 2004–7.
[39] R. Hann, "Uav icing: Ice accretion experiments and validation," 2019.
[40] F. A. Administration, "14 cfr parts 25 and 29, appendix c, icing design envelopes," 2002, dOT/FAA/AR-00/30.
[41] E. Whalen, A. Broeren, M. Bragg, and S. Lee, "Characteristics of runback ice accretions on airfoils and their aerodynamics effects," in *43rd AIAA Aerospace Sciences Meeting and Exhibit*, 2005, p. 1065.